IEEE Access
Multidisciplinary : Rapid Review : Open Access Journal

Received 7 July 2022, accepted 3 August 2022, date of publication 8 August 2022, date of current version 12 August 2022.
Digital Object Identifier 10.1109/ACCESS.2022.3197286

RESEARCH ARTICLE

Quasi-Phase-Matched Four-Wave Mixing Enabled by Grating-Assisted Coupling in a Hybrid Silicon Waveguide

MIN-SUK KWON
Department of Electrical Engineering, Ulsan National Institute of Science and Technology, Ulsan 44919, South Korea
e-mail: mskwon@unist.ac.kr

This work was supported in part by the Basic Science Research Program through the National Research Foundation of Korea (NRF) funded by the Ministry of Science, ICT and Future Planning under Grant NRF-2020R1A2C1102481, and in part by the Samsung Research Funding and Incubation Center for Future Technology under Grant SRFC-IT1901-07.

ABSTRACT Phase matching must be performed to realize four-wave mixing (FWM) in a silicon waveguide, which is challenging when a signal wavelength is highly deviated from an idler wavelength. To solve this problem, quasi-phase-matching (QPM) based on grating-assisted directional coupling (GADC) in a hybrid structure is theoretically investigated. The proposed system consists of a silicon strip with periodic width modulation as the grating and a silicon nitride strip that is vertically aligned to the silicon strip. GADC occurs between the TE_S mode (mainly confined in the silicon strip) and TE_N mode (mainly confined in the silicon nitride strip) at an idler wavelength. This phenomenon compensates for the phase mismatch occurring in FWM among the TE_S modes at the pump, signal, and idler wavelengths. Results of analysis of the hybrid structure show that the TE_S and TE_N modes at an idler wavelength of 2.1177 μm are efficiently generated with the TE_S modes at a pump wavelength of 1.58 μm and signal wavelength of 1.2601 μm. Moreover, the signal TE_S mode can be efficiently implemented with the pump TE_S mode and idler TE_N mode. Owing to the GADC characteristics, the conversion bandwidth of the signal is 0.8 nm; however, the signal wavelength can be thermally tuned, with a temperature change of 50 °C corresponding to a signal wavelength change of 3.6 nm. The hybrid structure with the GADC-based QPM can be used to generate and detect mid-infrared light with well-developed O-band and L-band devices.

INDEX TERMS Integrated optics, Kerr effect, nonlinear optical devices, silicon photonics.

I. INTRODUCTION

Four-wave mixing (FWM) is a third-order nonlinear optical interaction enabled by the Kerr nonlinearity, in which two photons are annihilated to generate two new photons. Silicon (Si) has a large nonlinear refractive index (n_2), and Si photonic waveguides exhibit strong light confinement, owing to which, nonlinear optical interactions occur effectively in the waveguides. Therefore, FWM in Si photonic waveguides has been used for wavelength conversion or generation, parametric amplification, frequency comb generation, and photon-pair generation [1], [2], [3], [4], [5], [6], [7], [8]. FWM-based wavelength conversion or generation is a promising method of detecting or generating mid-infrared (mid-IR) light with a wavelength of more than 2 μm by using well-developed photodetectors (PDs) and laser diodes (LDs) operating at telecom wavelengths [6], [9], [10], [11], [12]. Mid-IR optoelectronic devices are not as commonly used as telecom PDs and LDs and often require extreme operation conditions (*e.g.*, cryogenic temperatures). Hence, FWM-based detection or generation may be a practical solution for mid-IR photonics at present.

In such approaches, detection or generation is performed by translating a mid-IR wavelength to a telecom wavelength or vice versa. Translation can be performed using FWM when phase matching can be realized for optical waves with considerably different wavelengths (ranging from 1.26 μm in the O band to more than 2 μm). In the case of degenerate

The associate editor coordinating the review of this manuscript and approving it for publication was Yang Yue.

FWM, which involves only one pump wavelength (λ_p), phase matching can be achieved over a wavelength range around λ_p or at a discrete signal wavelength (λ_s) by carefully designing the geometry of a Si waveguide to achieve appropriate dispersion characteristics. For example, if the zero dispersion wavelength of a Si waveguide is approximately λ_p, the phase-matched wavelength range can be a few tens to hundreds of nanometers wide [5], [10], [11]. However, if λ_s is considerably deviated from the idler wavelength (λ_i), with $\lambda_i = 1/(2/\lambda_p - 1/\lambda_s)$, the phase-matched wavelength range is not adequately wide to include λ_s and λ_i or phase matching cannot be realized even discretely at λ_s.

To solve the phase-matching problem, an intermodal phase-matching method [13] and various quasi-phase-matching (QPM) methods [14], [15], [16], [17], [18], [19], [20] have been employed in Si photonics. The intermodal phase-matching method is implemented in a multimode waveguide with large dimensions (*e.g.*, 2 μm $\times$ 243 nm), and different modes are selected for the phase matching and carry pump, signal, and idler light. QPM maintains power transfer from the pump light to the signal or idler light by periodically suppressing the reverse power transfer caused by the nonzero phase difference between the signal or idler light and nonlinear polarization at λ_s or λ_i, which corresponds to a phase mismatch. Several QPM methods have been established based on waveguide width modulation [14], [15], [16], [17], [18], [19]. A representative method is to compensate for the phase mismatch with the reciprocal lattice vector associated with the periodic width modulation [14], [15]. Another approach is to alternate two Si waveguide sections with different widths to ensure that the phase mismatches in the two sections have the same sign but different values [16]. Specifically, the section corresponding to the phase mismatch with a larger magnitude is made shorter to ensure that the reverse power transfer is weakened. Alternatively, the widths of two alternating waveguide sections can be selected such that the phase mismatch is positive in one section and negative in the other section [17], [18], [19]. In this manner, the total phase mismatch accumulated along one section can compensate for that along the other section such that the reverse power transfer is suppressed.

In addition to width modulation, symmetric directional coupling (SDC) can be used to realize QPM [20]. In SDC-based QPM, the coupling length of an SDC structure at λ_i is equal to half the coherence length corresponding to the phase mismatch [21], [22], [23]. In this case, the idler generated by FWM in one waveguide of the SDC structure has an additional π phase change owing to the coupling with the other waveguide over one coherence length. This change resets the total phase mismatch accumulated over the coherence length, and the idler can continue to expand. However, to realize the SDC-based QPM for efficient FWM, the coupling lengths at λ_p, λ_s, and λ_i must be simultaneously controlled [22], [23] because SDC can occur at every wavelength with a different coupling length. Consequently, the design of a symmetric directional coupler for the SDC-based QPM is challenging.

This study is aimed at theoretically investigating a hybrid Si structure to demonstrate that it can realize efficient FWM with considerably separate λ_s and λ_i through QPM based on grating-assisted directional coupling (GADC). The hybrid structure consists of a width-modulated Si strip and a silicon nitride (SiN) strip. The GADC-based QPM can overcome the design problem associated with the SDC-based QPM because the GADC between two different waveguides can be made occur only at λ_i. A simulation method is developed and used to analyze the hybrid structure. The analysis shows that the hybrid structure generates mid-IR idler light associated with pump light in the L band and signal light in the O band. The resulting difference between λ_s and λ_i is larger than those achieved using the existing QPM methods based on width modulation [14], [16], [17]. The hybrid structure exhibits three advantages: (1) The signal wavelength can be thermally tuned by 3.6 nm for a temperature change of 50 °C; (2) the idler can be easily extracted from the SiN strip because the pump coupled to the SiN strip is sufficiently suppressed as the pump and signal travel along the Si strip; and (3) the signal can be generated and used to detect the idler when the pump and idler are coupled to the Si and SiN strips, respectively. The hybrid structure based on the GADC-based QPM is expected to be useful for mid-IR generation and detection.

II. HYBRID STRUCTURE AND ANALYSIS METHOD

A. HYBRID STRUCTURE

The composite waveguide of the hybrid structure is composed of a Si strip with width w_S and height h_S and a SiN strip with width w_N and height h_N. The SiN strip is vertically aligned to the Si strip with a gap of width g. The strips are embedded in silicon dioxide (SiO_2). Such composite waveguides have been realized and studied [24], [25] but they have not been used for nonlinear optical applications. The hybrid structure and composite waveguide are schematically illustrated in Figs. 1(a) and (b), respectively. The waveguide supports the fundamental transverse-electric (TE) mode mainly confined in the Si strip (TE_S mode) and the higher-order TE mode mainly confined in the SiN strip (TE_N mode). The electric field profiles of the two modes for w_S = 565 nm, h_S = 220 nm, w_N = 1.2 μm, h_N = 600 nm, and g = 450 nm, calculated at a wavelength of 2.1179 μm by using an eigenmode solver (Mode, Lumerical Inc.), are shown in Fig. 1(c). The TE_S mode is similar to the fundamental TE mode of an isolated Si strip waveguide (*i.e.*, the composite waveguide without the SiN strip). The TE_N mode is similar to the fundamental TE mode of an isolated SiN strip waveguide (*i.e.*, the composite waveguide without the Si strip), although a small part of its electric field exists around the Si strip. This phenomenon can be verified using the confinement factor of a waveguide mode [26]. The confinement factors of the TE_N mode in the SiN and Si strips are 68.7 % and 2.02 %, respectively.

In the hybrid structure, the coupling between the TE_S and TE_N modes can be achieved around a specific wavelength

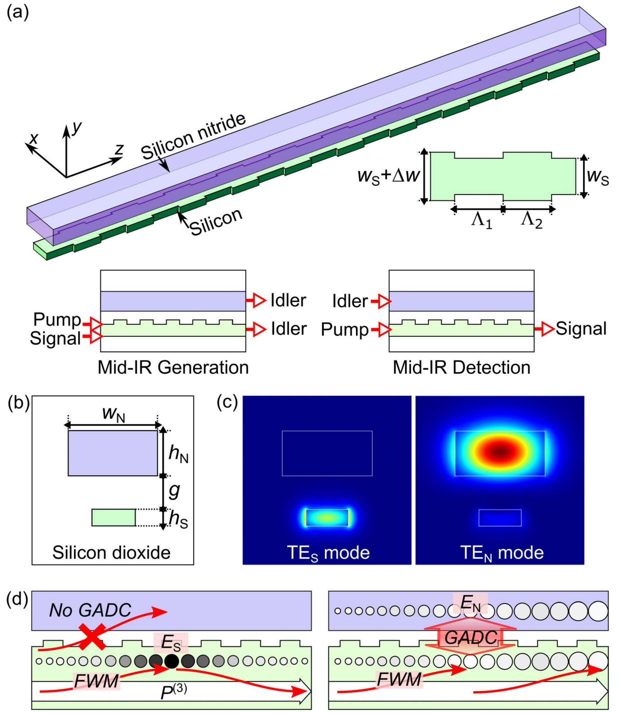

FIGURE 1. (a) Schematic of the hybrid structure. The width-modulated Si strip and SiN strip are embedded in SiO_2. The width of the Si strip alternates between w_S and $w_S + \Delta w$. The lower left and right panels illustrate mid-IR generation and detection, respectively. (b) Cross-section of the composite waveguide. (c) Mode profiles at a wavelength of 2.1179 μm. The squared magnitude of the electric field of the TE$_S$ (TE$_N$) mode is shown in the left (right) panel. (d) Operation mechanism. The circles represent the electric fields of the TE$_S$ and TE$_N$ modes (E_S and E_N), and the white arrows represent the nonlinear polarization $P^{(3)}$. The circle color is black when the net phase difference between E_S and $P^{(3)}$is π. In the left panel, without the GADC, E_S increases owing to the FWM and decreases because the phase mismatch or net phase difference is π at the coherence length. In the right panel, the GADC causes the net phase difference to be small. Consequently, the FWM efficiently increases E_S, and the GADC increases E_N.

by using a uniform grating of period Λ. The grating is implemented through the width modulation of the Si strip. In the grating region of length L_g, the Si strip width alternates between w_S and $w_S + \Delta w$. The length of section 1 (2) with the Si strip of width w_S ($w_S + \Delta w$) is Λ_1 (Λ_2), and $\Lambda_1 + \Lambda_2 = \Lambda$. The pump at λ_p in the L band and signal at λ_s in the O band propagate in the hybrid structure in the form of the TE$_S$ mode. The idler at λ_i travels in the form of the TE$_S$ or TE$_N$ mode. FWM among the pump, signal, and idler TE$_S$ modes occurs in the Si strip. Λ is adjusted to ensure that the GADC between the TE$_S$ and TE$_N$ modes occurs at λ_i. As illustrated in Fig. 1(d), when the GADC is weak or inefficient at wavelengths different from λ_i, the electric field of the TE$_S$ mode (E_S) increases and decreases because the phase mismatch between E_S and the nonlinear polarization $P^{(3)}$ is π at the coherence length. The GADC helps the idler TE$_S$ mode achieve an additional phase to compensate for the phase mismatch and routes the idler between the Si and SiN strips. Therefore, both E_S and the electric field of the TE$_N$ mode (E_N) increase as shown in Fig. 1(d). For mid-IR generation, the idler TE$_S$ and TE$_N$ modes are generated by the pump and signal TE$_S$ modes. For mid-IR detection, the signal TE$_S$ mode is generated by the pump TE$_S$ mode and idler TE$_N$ mode.

B. ANALYSIS METHOD

The analysis method used in this study consists of two steps: First, the nonlinear coupled-mode equations (NCMEs) in each section are solved, and second, mode matching is performed at each interface between the two sections. The NCMEs are explained in Appendix and similar to those for FWM in conventional Si waveguides [16]. The NCMEs are solved to determine the evolution of the pump, signal, and idler TE$_S$ modes in each section. When the amplitudes of the TE$_S$ and TE$_N$ modes in section l are represented by $A_{lS(\nu)}(z)$ and $A_{lN(\nu)}(z)$, where ν is p, s, and i, in each interval $(n\Lambda, n\Lambda + \Lambda_1]$ (section 1), $A_{1S(\nu)}(n\Lambda + \Lambda_1)$ is determined solving the NCMEs with $A_{1S(\nu)}(n\Lambda)$ for $\nu =$ p, s, and i used as initial values. In the next interval $(n\Lambda+\Lambda_1, n\Lambda+\Lambda]$ (section 2), $A_{2S(\nu)}(n\Lambda + \Lambda)$ is determined with $A_{2S(\nu)}(n\Lambda + \Lambda_1)$ for $\nu =$ p, s, and i used as initial values. In solving the NCMEs, z is a local coordinate that changes from 0 to Λ_1 (Λ_2) in section 1 (2). The ode45 solver of MATLAB, which is based on an explicit Runge–Kutta formula, is used to solve the NCMEs.

Mode matching is performed to determine the amplitudes of the TE$_S$ and TE$_N$ modes immediately after each interface with those immediately before the interface. In particular, at the interface $z = n\Lambda + \Lambda_1$, $A_{2S(\nu)}(n\Lambda + \Lambda_1)$ and $A_{2N(\nu)}(n\Lambda + \Lambda_1)$ are derived from $A_{1S(\nu)}(n\Lambda + \Lambda_1)$ and $A_{1N(\nu)}(n\Lambda + \Lambda_1)$as

$$\begin{bmatrix} A_{2S(\nu)}(n\Lambda+\Lambda_1) \\ A_{2N(\nu)}(n\Lambda+\Lambda_1) \\ A_{23(\nu)}(n\Lambda+\Lambda_1) \\ A_{24(\nu)}(n\Lambda+\Lambda_1) \\ \vdots \\ A_{2M(\nu)}(n\Lambda+\Lambda_1) \end{bmatrix} = \mathbf{T}_{12(\nu)}\mathbf{P}_{1(\nu)} \begin{bmatrix} A_{1S(\nu)}(n\Lambda+\Lambda_1) \\ A_{1N(\nu)}(n\Lambda+\Lambda_1) \\ A_{13(\nu)}(n\Lambda+\Lambda_1) \\ A_{14(\nu)}(n\Lambda+\Lambda_1) \\ \vdots \\ A_{1M(\nu)}(n\Lambda+\Lambda_1) \end{bmatrix}, \tag{1}$$

where $\mathbf{T}_{12(\nu)}$ is the transmission matrix from section 1 to section 2 at λ_ν, and $\mathbf{P}_{1(\nu)}$ is the propagation matrix in section 1 at λ_ν. $\mathbf{P}_{1(\nu)}$ is a diagonal matrix, the (1, 1), (2, 2), and (i, i) elements of which are $\exp(-j2\pi\tilde{n}_{1S(\nu)}\Lambda_1/\lambda_\nu)$, $\exp(-\alpha_{1N(\nu)}\Lambda_1/2 - j2\pi\tilde{n}_{1N(\nu)}\Lambda_1/\lambda_\nu)$, and $\exp(-\alpha_{1i(\nu)}\Lambda_1/2 - j2\pi\tilde{n}_{1i(\nu)}\Lambda_1/\lambda_\nu)$ for $i = 3, \ldots, M$, respectively. M is the number of modes present in each composite waveguide (*i.e.*, section 1 or 2) bounded by perfect electric walls, which can ensure the correctness of mode matching. In the following simulation, the dimensions of the bounded domain are 8 μm $\times$ 8 μm, and M is 20. $\alpha_{lS(\nu)}$ and $\tilde{n}_{lS(\nu)}$ ($\alpha_{lN(\nu)}$ and $\tilde{n}_{lN(\nu)}$) are the linear absorption coefficient and effective index of the TE$_S$ (TE$_N$) mode in section l at λ_ν, respectively. $\alpha_{li(\nu)}$ and $\tilde{n}_{li(\nu)}$ are the corresponding values of mode i in section l. Notably, (1) is correct only when reflections from the interface are negligible. Findings indicate that the total reflected power for the TE_S or TE_N mode is $\sim 10^{-3}$ % of the incident power if Δw is smaller than 100 nm. At the interface $z = n\Lambda + \Lambda$, similar to (1), the relation of $A_{1S(\nu)}(n\Lambda + \Lambda)$ and $A_{1N(\nu)}(n\Lambda + \Lambda)$ to $A_{2S(\nu)}(n\Lambda + \Lambda)$ and $A_{2N(\nu)}(n\Lambda + \Lambda)$ can be expressed as

$$\begin{bmatrix} A_{1S(\nu)}(n\Lambda + \Lambda) \\ A_{1N(\nu)}(n\Lambda + \Lambda) \\ A_{13(\nu)}(n\Lambda + \Lambda) \\ A_{14(\nu)}(n\Lambda + \Lambda) \\ \vdots \\ A_{1M(\nu)}(n\Lambda + \Lambda) \end{bmatrix} = \mathbf{T}_{21(\nu)}\mathbf{P}_{2(\nu)} \begin{bmatrix} A_{2S(\nu)}(n\Lambda + \Lambda) \\ A_{2N(\nu)}(n\Lambda + \Lambda) \\ A_{23(\nu)}(n\Lambda + \Lambda) \\ A_{24(\nu)}(n\Lambda + \Lambda) \\ \vdots \\ A_{2M(\nu)}(n\Lambda + \Lambda) \end{bmatrix}, \tag{2}$$

where $\mathbf{T}_{21(\nu)}$ is the transmission matrix from section 2 to section 1 at λ_ν, and $\mathbf{P}_{2(\nu)}$ is the propagation matrix in section 2 at λ_ν. $\mathbf{P}_{2(\nu)}$ is a diagonal matrix, the (1, 1), (2, 2), and (i, i) elements of which are $\exp(-j2\pi\tilde{n}_{2S(\nu)}\Lambda_2/\lambda_\nu)$, $\exp(-\alpha_{2N(\nu)}\Lambda_2/2 - j2\pi\tilde{n}_{2N(\nu)}\Lambda_2/\lambda_\nu)$, and $\exp(-\alpha_{2i(\nu)}\Lambda_2/2 - j2\pi\tilde{n}_{2i(\nu)}\Lambda_2/\lambda_\nu)$ for $i = 3, \ldots, M$, respectively. To use (1) and (2), the transmission matrices $\mathbf{T}_{12(\nu)}$ and $\mathbf{T}_{21(\nu)}$ are calculated at the interface between the composite waveguides with the Si strips of width w_S and $w_S + \Delta w$ by using the eigenmode expansion (EME) method incorporated in the Mode software. The two steps: solving the NCMEs in each section, and mode matching at each interface, are alternately repeated over the grating region of length L_g (n increases from 0 to L_g/Λ).

III. SIMULATION RESULTS

A. PHASE MISMATCH IN THE UNIFORM COMPOSITE WAVEGUIDE

The total phase mismatch associated with the FWM in section l is the sum of the linear phase mismatch $\Delta\beta_{lS}$ and nonlinear phase mismatch determined by the free-carrier index change, self-phase modulation, and cross-phase modulation. The linear phase mismatch in section l, $\Delta\beta_{lS}$ can be expressed as $\Delta\beta_{lS} = 2\pi\left(2\tilde{n}_{lS(p)}/\lambda_p - \tilde{n}_{lS(s)}/\lambda_s - \tilde{n}_{lS(i)}/\lambda_i\right)$. Usually, the nonlinear phase mismatch is considerably smaller than $\Delta\beta_{lS}$, and the total phase mismatch is mainly determined by $\Delta\beta_{lS}$. To examine whether phase matching can be achieved in the uniform composite waveguide, $\Delta\beta_{1S}$ is calculated for various values of w_S, w_N, h_N, and g when λ_p, λ_s, and λ_i are 1.58 μm, 1.26 μm, and 2.1179 μm, respectively. h_S is set at 220 nm, which is the Si layer thickness of silicon-on-insulator (SOI) wafers typically used in Si photonics. The refractive index of SiN is extracted from [27], and the Lorentz model in Mode is used to determine the refractive indices of Si and SiO_2. At a wavelength of 1.55 μm, the refractive indices of SiN, Si, and SiO_2 are 2.0192, 3.4734, and 1.4433, respectively.

The calculated relations of $\Delta\beta_{1S}$ to w_S are shown in Fig. 2 ($\Delta\beta_{2S}$ can also be determined from Fig. 2 as w_S equals $w_S + \Delta w$): $\Delta\beta_{1S}$ never approaches zero regardless of the values of w_S, w_N, h_N, and g. The TE_S mode at a shorter wavelength is more strongly confined in the Si strip. Thus, when w_S increases from 550 nm to 650 nm, $\tilde{n}_{1S(s)}$ slightly increases. $\tilde{n}_{1S(p)}$ first increases rapidly and later increases slowly. $\tilde{n}_{1S(i)}$ rapidly increases. Consequently, $\Delta\beta_{1S}$ increases and then decreases as w_S increases. The SiN strip affects the idler TE_S mode more notably than the pump and signal TE_S modes, and $\tilde{n}_{1S(i)}$ increases to a larger extent with an increase in w_N or h_N or with a decrease in g than $\tilde{n}_{1S(s)}$ and $\tilde{n}_{1S(p)}$. Hence, $\Delta\beta_{1S}$ decreases as w_N or h_N increases (notably, the values of w_N and h_N in Fig. 2(a) are chosen only for demonstration, and the dependence of $\Delta\beta_{1S}$ on w_N or h_N has been confirmed for other values). In addition, $\Delta\beta_{1S}$ decreases as g decreases. When g is extremely large, $\Delta\beta_{1S}$ approaches the linear phase mismatch of the isolated Si strip waveguide, which is never equal to zero. Fig. 2 indicates that the phase matching for the FWM among the pump at 1.58 μm, signal at 1.26 μm, and idler at 2.1179 μm cannot be achieved in either the composite waveguide or the isolated Si strip waveguide when the Si strip is 220 nm thick. As shown in the following analysis, the GADC-based QPM can facilitate the efficient occurrence of FWM in the hybrid structure, in which the nonzero phase mismatches in sections 1 and 2 are compensated by the GADC.

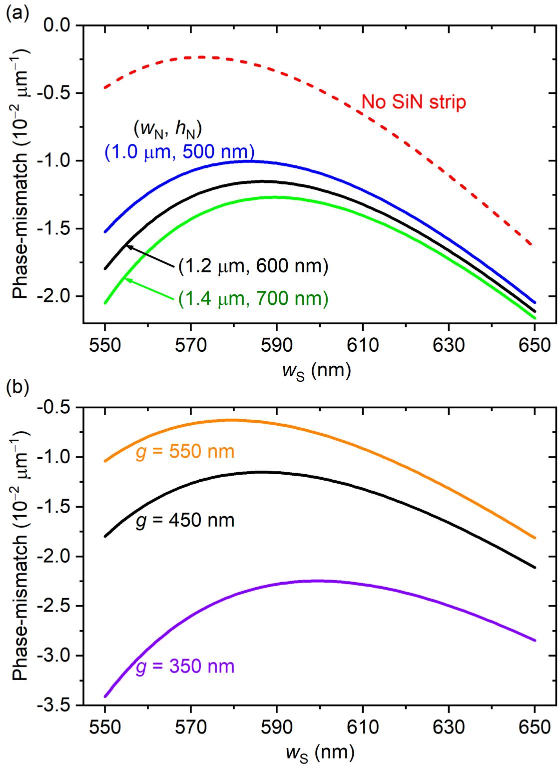

FIGURE 2. Relations of the phase mismatch $\Delta\beta_{1S}$ to w_S for several values of w_N, h_N, and g. The relation of the isolated Si strip waveguide (red dashed line) is also shown. The curves in (a) and (b) are calculated for g = 450 nm and w_N = 1.2 μm and h_N = 600 nm, respectively.

B. DESIGN OF THE HYBRID STRUCTURE

The design is to determine the values of w_S, w_N, h_N, g, and Δw such that the idler TE_S and TE_N modes at λ_i = 2.1179 μm are efficiently generated by the pump TE_S mode at $\lambda_p = 1.58\ \mu$m and signal TE_S mode at $\lambda_s = 1.26\ \mu$m. First, w_S, w_N, h_N, and g are determined to satisfy the aforementioned relation between the coupling and coherence lengths. Then, Δw is determined considering conversion efficiencies to the idler TE_S and TE_N modes. The coupling length l_c of the GADC is compared with the average coherence length L_c of the FWM in the hybrid structure, which is defined as

$$L_c \pi / \left(|\Lambda_1 \Delta\beta_{1S} + \Lambda_2 \Delta\beta_{2S}| / \Lambda\right). \tag{3}$$

The values of w_S, w_N, h_N, and g are selected such that the value of Δw for which $l_c = L_c/2$ is small. If $l_c = L_c/2$, at distance L_c, the phase change that the idler TE_S mode gains owing to the GADC and phase mismatch between the idler TE_S mode and nonlinear polarization are equal to π, which is illustrated in Fig. 1(d). As verified in the following analysis, this phenomenon causes both the idler TE_S and TE_N modes to be similarly efficiently generated. Furthermore, Δw must be adequately small to minimize the scattering loss from the grating. For the design and following simulation, the initial powers of the pump and signal TE_S modes are assumed to be 300 mW and 100 μW, respectively [16], [17]. The corresponding values for the idler TE_S mode and all the TE_N modes are set at zero. In addition, the linear absorption coefficients $\alpha_{lS(\nu)}$, $\alpha_{lN(\nu)}$, and $\alpha_{li(\nu)}$are set as 1.5 dB/cm [16], [17] regardless of l, i, and ν, and L_g is set as 10 mm.

Λ_1, Λ_2, and coupling length l_c are determined using the EME method incorporated in Mode as follows. Λ_1 and Λ_2 are initially estimated using $\lambda_i/[\tilde{n}_{lS(i)} - \tilde{n}_{lN(i)}]$, $l = 1$ and 2, and optimized to ensure that the power carried by the TE_S mode is maximally transferred to the TE_N mode at λ_i (the power transfer from the TE_S mode to the TE_N mode is confirmed to be negligible at λ_p and λ_s). In this case, l_c is the distance over which the TE_S mode power is minimized and TE_N mode power is maximized. The determined relations of l_c to Δw for several values of w_S, w_N, h_N, and g are shown in Fig. 3. For the calculation, h_S is set as 220 nm. Half the coherence length, $L_c/2$, is also shown in Fig. 3. Depending on w_S, w_N, h_N, g, and Δw, $\Lambda_1$changes between 2.554 and 3.993 μm and Λ_2 changes between 1.196 and 3.535 μm. As Δw increases, l_c decreases owing to the stronger coupling, and L_c decreases gradually because $|\Delta\beta_{2S}|$ increases when w_S is approximately 565 nm. When w_S increases, the coupling becomes weak because the idler TE_S mode is more confined in the Si strip, and the l_c curve shown in Fig. 3(a) moves upward. However, $|\Delta\beta_{1S}|$ decreases, $|\Delta\beta_{2S}|$ increases, and the $L_c/2$ curve does not change clearly. Hence, the value of Δw for which $l_c = L_c/2$ increases as w_S increases. When w_N and h_N increase, the coupling becomes weak because the idler TE_N mode is more confined in the SiN strip, and the l_c curve shown in Fig. 3(b) moves slightly upward. In contrast, $|\Delta\beta_{1S}|$ and $|\Delta\beta_{2S}|$ increase, as indicated in Fig. 2(a), and the $L_c/2$ curve moves downward. Hence, the value of Δw for which $l_c = L_c/2$ increases as w_N and h_N increase. When g increases, the coupling becomes weak, and $|\Delta\beta_{1S}|$ and $|\Delta\beta_{2S}|$ decrease, as shown in Fig. 2(b). Therefore, both the l_c and $L_c/2$ curves in Fig. 3(c) move upward. L_c is more affected by

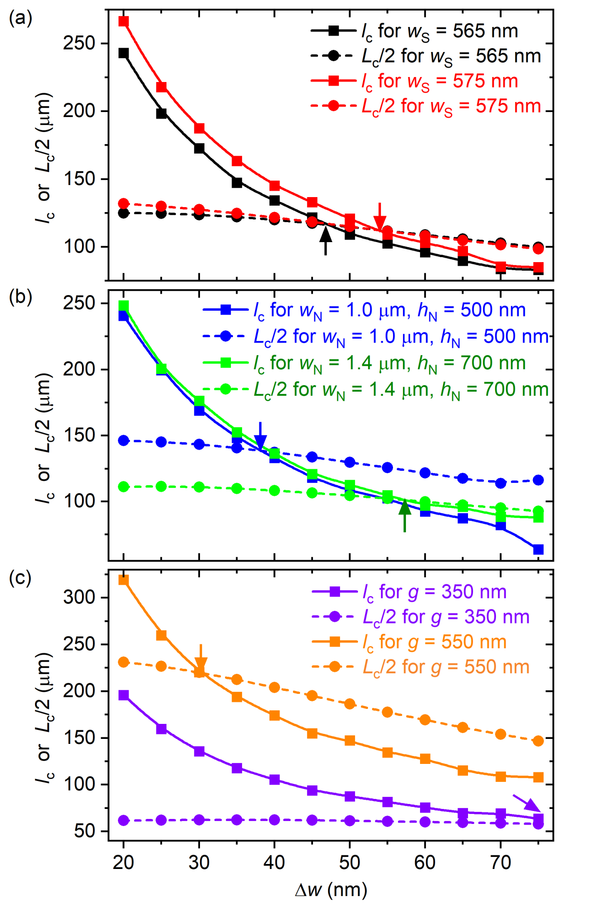

FIGURE 3. Relations of the coupling length l_c to Δw for several values of w_S, w_N, h_N, and g. The coupling length (represented by squares with a solid line) is compared to half the coherence length L_c (represented by circles with a dashed line). The relations in (a) are calculated for w_N = 1.2 μm, h_N = 600 nm, and g = 450 nm; those in (b) are calculated for w_S = 565 nm and g = 450 nm; and those in (c) are calculated for w_S = 565 nm, w_N = 1.2 μm, and h_N = 600 nm. The arrows indicate the intersections between the l_c and $L_c/2$ curves.

g than l_c, and the value of Δw for which $l_c = L_c/2$ decreases as g increases. w_N and h_N must be adequately small to ensure that Δw is small. However, these values must be adequately large to effectively confine the idler TE_N mode in the SiN strip. In addition, if h_N is excessively large, the deposition of a thick SiN layer may be challenging. These aspects must be considered when selecting the values of w_S, w_N, h_N, and g for the hybrid structure. For the hybrid structure simulated in this study, $w_S = 565$ nm, $w_N = 1.2\ \mu$m, $h_N = 600$ nm, and $g = 450$ nm.

To finally determine Δw, the conditions in which the GADC-based QPM is best achieved and the optimality of the value of Δw for which $l_c = L_c/2$ must be examined. To this end, the hybrid structure with Δw ranging from 20 nm to 75 nm is simulated. $\Lambda_1 = 3.189\ \mu$m, and Λ_2 decreases from 2.889 μm to 2.388 μm as Δw increases from 20 nm to 75 nm (Fig. 4(a)). The output powers of the idler TE_S and TE_N modes are calculated for λ_s varying around 1.26 μm with $\lambda_p = 1.58\ \mu$m (λ_i is determined by λ_s and λ_p), and

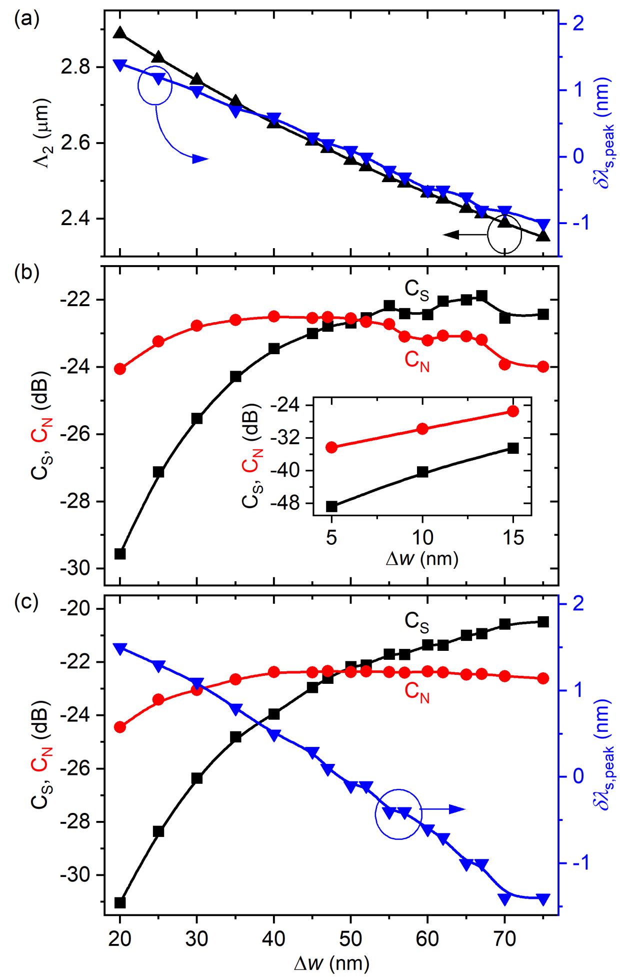

FIGURE 4. Generation of the idler TE modes with the pump and signal TE_S modes. (a) Relations of Λ_2 and $\delta\lambda_{s,peak}$, which is the difference of 1.26 μm from $\lambda_{s,peak}$, with Δw. (b) and (c) Relations of the conversion efficiencies C_S and C_N to Δw. C_S and C_N in (b) are obtained using the analysis method described in Section II.B. The inset of (b) shows C_S and C_N for Δw = 5, 10, and 15 nm. The corresponding values in (c) are obtained by solving the compound coupled-mode equations in (4). $\delta\lambda_{s,peak}$ in this case is also shown, which is slightly different from $\delta\lambda_{s,peak}$ in (a). All the relations are calculated for w_S = 565 nm, w_N = 1.2 μm, h_N = 600 nm, g = 450 nm, and Λ_1 = 3.189 μm.

the maximum power of the idler TE_S mode is determined. The signal wavelength for which the maximum power occurs, $\lambda_{s,peak}$, is shown as a function of Δw in Fig. 4(a). $L_c/2 = l_c$ for $\Delta w \cong 47$ nm, as shown in Fig. 3, and $\lambda_{s,peak}$ is approximately 1.26 μm at $\Delta w = 50$ nm. l_c is larger (smaller) than $L_c/2$ for Δw smaller (larger) than 47 nm. Because L_c increases with λ_s, $\lambda_{s,peak}$ tends to increase (decrease) for $\Delta w < (>)$ 47 nm to decrease the difference between l_c and $L_c/2$.

The efficiency of conversion to the idler TE_S (TE_N) mode, denoted by C_S (C_N), can be obtained by dividing the output power of the idler TE_S (TE_N) mode for $\lambda_{s,peak}$ by the initial power of the signal TE_S mode. The relations of C_S and C_N with Δw are shown in Fig. 4(b). C_S obtained from the uniform composite waveguide without the grating is -52.4 dB when the waveguide length is 9.925 mm and λ_s is 1.26 μm (in this case, C_N is $-\infty$ dB because the GADC does not exist). Compared to this value, C_S and C_N shown in Fig. 4(b) are considerably larger, which indicates that the GADC-based QPM is useful for increasing the conversion efficiency. The C_N curve exhibits a plateau for Δw ranging from 40 to 50 nm, and C_N decreases for Δw beyond this range. C_S increases with Δw if $\Delta w \leq 55$ nm, but it does not increase significantly when $\Delta w > 55$ nm. The C_S and C_N curves intersect at $\Delta w \cong 50$ nm, and both C_S and C_N exhibit the same large value of -22.6 dB at $\Delta w = 50$ nm. In accordance, the GADC-based QPM can be considered to be best achieved when Δw approximately satisfies the relation $l_c = L_c/2$. The optimal value of Δw for the best QPM is only slightly different from that for $l_c = L_c/2$, partly, owing to the nonlinear phase mismatch. When the nonlinear phase mismatch is considered, L_c decreases by $\sim$0.9 % from the value shown in Fig. 3. Interestingly, as shown in the inset of Fig. 4(b), when Δw decreases from 20 nm to 5 nm, C_S decreases and approaches the value obtained from the uniform composite waveguide whereas C_N decreases to a non-negligible value of -34.3 dB. For $\Delta w = 5$ nm, l_c is 925 μm, which is considerably larger than $L_c/2$, and the GADC-based QPM is ineffective. Over the 10-mm-long grating region, the TE_S mode power generated by the FWM is continually transferred to the TE_N mode, and C_N reaches -34.3 dB.

To perform a comparative analysis, C_S and C_N are calculated by solving compound coupled-mode equations, which simultaneously govern the nonlinear coupling among the pump, signal, idler TE_S modes and linear coupling between the TE_S and TE_N modes in the composite waveguide with the Si strip of width w_S. The equations are

$$\frac{\mathrm{d}A_{1S(\nu)}}{\mathrm{d}z} = f_{1(\nu)}\left[A_{1S(p)}, A_{1S(s)}, A_{1S(i)}\right] - j\kappa_\nu A_{1N(\nu)} \exp\left(j\Delta\beta_{g(\nu)}z\right), \quad (4a)$$

$$\frac{\mathrm{d}A_{1N(\nu)}}{\mathrm{d}z} = -\frac{1}{2}\alpha_{1N(\nu)}A_{1N(\nu)} - j\kappa_\nu A_{1S(\nu)} \exp\left(-j\Delta\beta_{g(\nu)}z\right), \quad (4b)$$

for ν = p, s, and i, where $f_{l(\nu)}[\cdots]$ pertains to the right-hand side of the NCMEs (see (6) in Appendix), and κ_ν is the coupling coefficient between the TE_S and TE_N modes at λ_ν. $\Delta\beta_{g(\nu)}$is the grating-related phase mismatch at λ_ν, defined as$\Delta\beta_{g(\nu)} = 2\pi\left(\tilde{n}_{1S(\nu)}/\lambda_\nu - \tilde{n}_{1N(\nu)}/\lambda_\nu - 1/\Lambda\right)$. The equations are solved using the ode45 solver with Λ set as $2\Lambda_1$. κ_i is defined as $\pi/(2l_c)$, and κ_p and κ_s are approximated by κ_i. The obtained C_S and C_N curves are shown in Fig. 4(c) along with $\lambda_{s,peak}$. The curves are similar to those shown in Fig. 4(b) when $\Delta w \leq 50$ nm. However, in the case shown in Fig. 4(c), C_S continually increases with Δw, and C_N decreases extremely gradually as Δw increases over 50 nm. Because the compound coupled-mode equations in (4) are based on the assumption that the TE_S and TE_N modes in the composite waveguide with the Si strip of width w_S are weakly perturbed by the grating, the results shown in Fig. 4(c) are less correct compared to those in Fig. 4(b) when Δw is

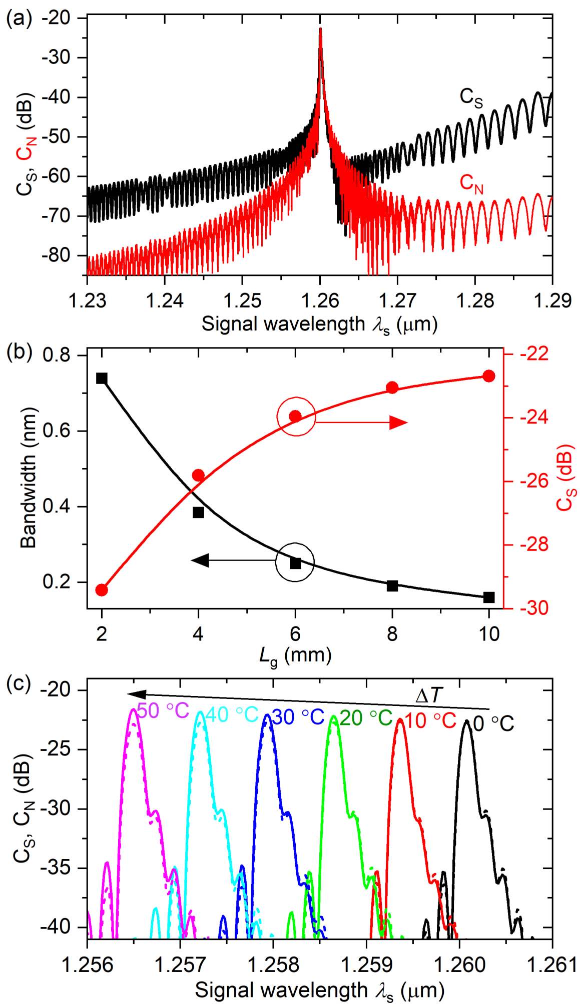

FIGURE 5. (a) Spectra of conversion efficiencies C_S and C_N for L_g = 10 mm. (b) Relation between the 3 dB bandwidth and L_g (black squares), and relation between C_S at $\lambda_{s,peak}$ with L_g (red circles). The solid lines are visual guides. (c) C_S (solid curves) and C_N (dashed curves) spectra for the temperature change ΔT = 0 °C to 50 °C. The C_S and C_N spectra blue-shift by 0.72 nm when the temperature of the hybrid structure increases by 10 °C. Δw = 50 nm, and Λ_2 = 2.554 μm; the other parameters are the same as those in the case shown in Fig. 4.

large. The increase in C_S assisted by the stronger GADC for $\Delta w > 50$ nm, shown in Fig. 4(c), is likely canceled by scattering losses from the interfaces between the sections, as shown in Fig. 4(b).

As shown in Appendix, the variations in C_S and C_N along the z axis may explain why C_S is smaller (larger) than C_N for $\Delta w < (>)$ 50 nm in Fig. 4(b). When $\Delta w < 50$ nm, the FWM does not efficiently generate the TE_S mode, but the generated power of the TE_S mode is continually transferred to the TE_N mode through the GADC. When $\Delta w > 50$ nm, the FWM efficiently generates the TE_S mode with the help of the strong GADC. Therefore, the most effective GADC-based QPM is attained for $\Delta w = 50$ nm because both C_S and C_N increase with z in a similar manner to nearly the same value, and Δw is determined to be 50 nm.

C. CHARACTERISTICS OF THE HYBRID STRUCTURE

The parameter values of the designed hybrid structure are as follows: w_S = 565 nm, w_N = 1.2 μm, h_N = 600 nm, g = 450 nm, Δw = 50 nm, Λ_1 = 3.189 μm, and Λ_2 = 2.554 μm. The C_S and C_N spectra are shown as functions of λ_s in Fig. 5(a) (λ_p is fixed at 1.58 μm, and λ_i changes with λ_s). The C_S spectrum is centered at 1.2601 μm. The full width at half maximum (FWHM) of the C_S spectrum is 0.16 nm, and that converted for λ_i is 0.44 nm. In general, the FWHM of the cross-over or straight-through transmission spectrum of a GADC structure is inversely proportional to the number of periods. In the case of the hybrid structure with L_g = 9.987 mm, which is an odd integer multiple of l_c, the number of periods is 1739, and its cross-over spectrum has an FWHM of 2.4 nm near λ_i = 2.1177 μm, which is converted to 0.87 nm for λ_s = 1.2601 μm, when no pump and signal TE_S modes exist. The FWHM of the C_S spectrum is small because the GADC-based QPM occurs within the FWHM of the GADC. The dependence of the conversion FWHM on L_g can be confirmed by Fig. 5(b). The conversion FWHM increases with decreasing L_g, and the maximum conversion efficiency decreases.

In Table 1, the characteristics of the FWM in the hybrid structure are compared with those of the previous FWMs based on the different phase matching methods. Notably, the difference between λ_s and λ_i of this FWM is second largest in Table 1. The SDC-based QPM can result in the largest difference, which is allowed only when all the pump, signal, and idler are carefully controlled to be the antisymmetric mode of the SDC structure. Because of the large difference, the magnitude of the phase mismatches is considerable. However, the GADC-based QPM enables the conversion efficiency (CE) of this FWM to be comparable to those of the other FWMs (actually, the net CE of this FWM amounts to −19.6 dB if both C_S and C_N are considered). Therefore, the GADC-based QPM is appropriate for conversion between more widely separate signal and idler wavelengths with a similar efficiency.

Owing to the narrow conversion FWHM, λ_s must match $\lambda_{s,peak}$ to generate the idler TE_S and TE_N modes. This stringent requirement may be bypassed to a certain extent through thermal tuning. Assuming that the hybrid structure is uniformly heated, and the materials have wavelength-independent thermo-optic coefficients, the C_S spectra are calculated for different temperatures. The thermo-optic coefficients of Si, SiN, and SiO_2 for the calculation are 1.8×10^{-4} K^{-1}, 2.51×10^{-5} K^{-1}, and 1.0×10^{-5} K^{-1}, respectively. As the temperature of the hybrid structure increases, the effective index of the idler TE_S mode increases more than that of the TE_N mode, and the idler wavelength at which the GADC between the idler TE_S and TE_N modes occurs increases. Therefore, $\lambda_{s,peak}$ decreases at a rate of 72 pm/K, and λ_s can be tuned by 3.6 nm, between 1.2601 μm and 1.2565 μm, when the temperature is adjusted by 50 °C. As shown in Fig. 5(c), the peak value of C_S increases with the temperature, but that of C_N decreases. This phenomenon

TABLE 1. Comparison of this FWM with the previous FWMs.

Phase matching method	Ref.	Length [mm]	Pump power [mW]	λ_s [μm]	λ_i [μm]	Phase mismatch [mm^{-1}]	CE [dB]	FWHM [nm]
Intermodal phase matching [a]	[13]	15	1000	1.469	1.640	0	– 14.7	4.7
QPM based on a grating-induced reciprocal vector	[14]	5	251	1.421	1.687	6.28	– 27	27
QPM based on phase mismatch switching	[16]	10	300	1.334	1.850	24.6 / 4.58 [b]	– 21.7	17.8
QPM based on phase mismatch compensation	[17]	15	300	1.402	1.733	–7.49 / 5.57 [c]	– 17.4	331
QPM based on symmetric directional coupling [e]	[20]	5	NA	1.170	2.297	NA	NA	0.23
GADC-based QPM	This work	10	300	1.260	2.118	–13.5 / –13.9 [d]	– 22.6	0.16

[a]In this case, the experimentally used or measured values are shown in the table.
[b]When the Si strip is 600 (720) nm wide, the phase mismatch is 24.6 (4.58) mm^{-1}.
[c]When the Si strip is 695 (815) nm wide, the phase mismatch is –7.49 (5.57) mm^{-1}.
[d]When the Si strip is 565 (615) nm wide, the phase mismatch is –13.5 (–13.9) mm^{-1}.
[e]In this case, all the pump, signal, and idler are the antisymmetric mode of the SDC structure in which the gap between the identical Si strips is 480 nm wide.

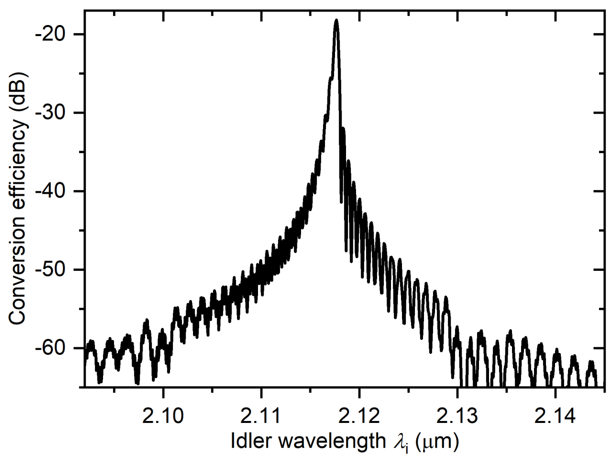

FIGURE 6. Generation of the signal TE_S mode with the pump TE_S mode and idler TE_N mode. The conversion efficiency from the idler TE_N mode to the signal TE_S mode is shown as a function of the idler wavelength λ_i.

occurs because l_c decreases with increasing λ_i. Subsequently, l_c becomes smaller than $L_c/2$, and C_S (C_N) is larger (smaller) than the corresponding value in the case of $l_c \approx L_c/2$ (*i.e.*, no temperature increase), as deduced from the results shown in Fig. 4(b).

The peak generated power of the idler TE_N mode at $\lambda_i = 2.1177$ μm is 0.561 μW. This value is comparable to the power of the pump TE_N mode, which rapidly oscillates between 0.5 μW and 1.5 μW depending on L_g. In contrast, the power of the idler TE_S mode is approximately five orders of magnitude smaller than that of the pump TE_S mode. Therefore, the separation of the idler TE_N mode from the pump TE_N mode in the SiN strip is more effective than that of the idler TE_S mode from the pump TE_S mode in the Si strip.

The hybrid structure is useful for not only mid-IR generation (*i.e.*, generation of the idler TE_N mode) but also mid-IR detection. To demonstrate the latter aspect, the hybrid structure is operated in a different manner: The idler TE_N mode with a power of 100 μW and pump TE_S mode with a power of 300 mW are input to the hybrid structure, and the signal TE_S mode is generated. The power of the generated signal TE_S mode is calculated with respect to λ_i (λ_p is fixed as 1.58 μm, and λ_s changes with λ_i). The conversion efficiency from the idler TE_N mode to the signal TE_S mode is calculated by dividing the power by the initial power of the idler TE_N mode, and it is shown in Fig. 6. The conversion efficiency is largest at $\lambda_i = 2.1177$ μm, which corresponds to $\lambda_s = 1.2601$ μm. The peak conversion efficiency is 4.4 dB larger than the peak value of C_S or C_N in Fig. 5(a). This phenomenon occurs because the signal TE_S mode is not coupled to the signal TE_N mode via the grating. The mid-infrared spectrum ranging between 2.1177 μm and 2.1279 μm may be analyzed by controlling the temperature of the hybrid structure within 50 °C and detecting the generated signal TE_S mode with an O-band photodetector.

D. PROBLEMS IN REALIZING THE HYBRID STRUCTURE

First, the tolerance of the characteristics of the hybrid structure on the fabrication errors is examined. w_S sensitively influences the effective index of the TE_S mode. g can be different from the designed value because the intermediate SiO_2 is prepared through deposition and chemical-mechanical polishing. Thus, the tolerances for w_S and g are considered. In addition, the alignment between the Si and SiN strips may be inaccurate, and the tolerance for the alignment is considered. To determine $\lambda_{s,peak}$, the C_S and C_N spectra are obtained for changes in w_S (Δw_S), g (Δg), or horizontal center-to-center distance between the Si and SiN strips, d.

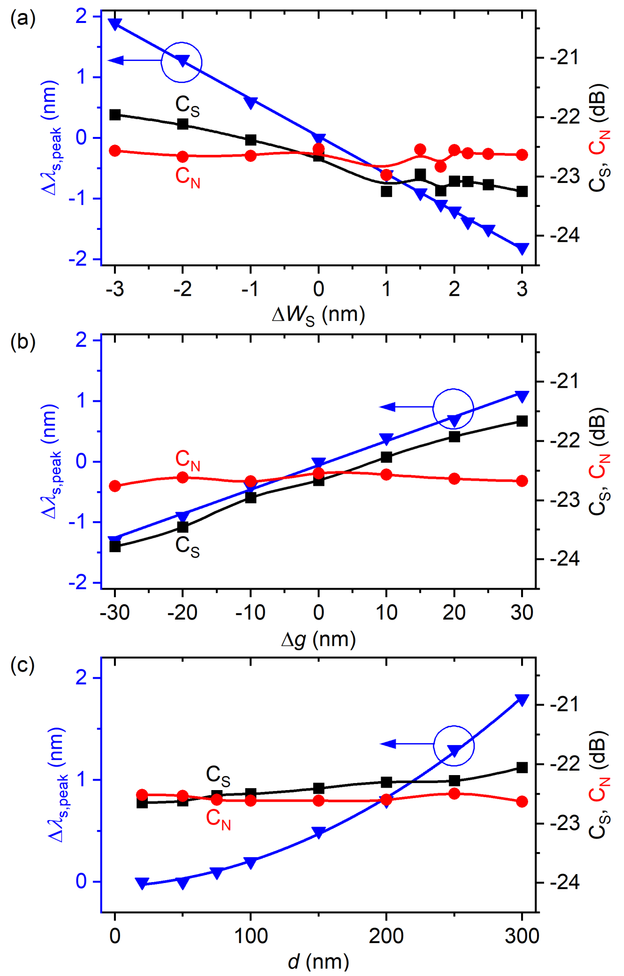

FIGURE 7. Changes in $\lambda_{s,peak}$, $\Delta\lambda_{s,peak}$ (blue inverted triangles), and C_S and C_N values at $\lambda_{s,peak}$ (black squares and red circles) depending on (a) changes in w_S (Δw_S), (b) changes in g (Δg), or (c) horizontal center-to-center distance between the Si and SiN strips, d. The blue straight lines in (a) and (b) are fitted to the relations of $\Delta\lambda_{s,peak}$ to Δw_S and Δg, respectively. The quadratic curve in (c) is fitted to the relation of $\Delta\lambda_{s,peak}$ to d. The black and red curves related to C_S and C_N are visual guides.

The difference between $\lambda_{s,peak}$ and 1.2601 μm ($\lambda_{s,peak}$ for $\Delta w_S = 0$ nm, $\Delta g = 0$ nm, and $d = 0$ nm), $\Delta\lambda_{s,peak}$, is shown as a function of Δw_S, Δg, or d in Fig. 7. In addition, the C_S and C_N values at $\lambda_{s,peak}$ are shown in Fig. 7. $\Delta\lambda_{s,peak}$ changes almost linearly depending on Δw_S or Δg. The slopes of the straight lines fitted to the relations of $\Delta\lambda_{s,peak}$ to Δw_S and Δg are -0.62 nm/nm and 0.04 nm/nm, respectively. $\Delta\lambda_{s,peak}$ increases nearly quadratically with d and is smaller than 1 nm even for $d = 200$ nm. Whereas the C_S and C_N spectra clearly shift by a few nanometers (considerably larger than the 3-dB bandwidth), the values at $\lambda_{s,peak}$ do not change significantly. Consequently, w_S must be strictly controlled, which is a typical requirement for Si photonic devices such as micro-ring resonators. However, the tolerances for g and d are considerably larger than that for w_S.

If the realization of the hybrid structure is carried out using standard CMOS fabrication processes such as 193 nm optical lithography, the standard deviation of Si line width changes is 2.6 nm on an 8-inch SOI wafer on which the Si film thickness varies with a standard deviation of 2 nm [28]. Similar to the dependence of $\lambda_{s,peak}$ on w_S, as the Si strip height h_S increases, $\lambda_{s,peak}$ linearly decreases with a change rate of -2.24 nm/nm. Therefore, when the hybrid structure is realized, actual $\lambda_{s,peak}$ could be different from designed $\lambda_{s,peak}$ by a few nanometers owing to changes in the Si strip width and height. $\Delta\lambda_{s,peak}$ owing to the fabrication errors could be partly offset with the aforementioned thermal tuning.

Second, the actual loss of the TE_S mode in the structure owing to scattering from the grating is examined. The loss can be estimated with reference to a silicon photonic distributed feedback resonator filter that consists of Bragg gratings and half-wave spacers [29]. When the Si strip width of the realized filter alternates between 470 and 530 nm and the total number of periods of all the Bragg gratings is 1235, the filter has a transmission loss of ~2.8 dB near 1.538 μm. Because the number of periods of the hybrid structure is 1741, its loss may be similar to this value. To decrease the loss, the grating can be formed along the SiN strip rather than the Si strip. In this case, the coupling between the TE_S and TE_N mode is weakened owing to the strong confinement of the TE_S mode. For example, when the SiN strip width alternates between 1.2 and 1.4 μm, the coupling length l_c is 494 μm, which is slightly larger than that for $\Delta w = 10$ nm, and the peak C_S and C_N values are -43 and -31 dB, respectively. Therefore, the SiN strip width modulation is not appropriate for the current hybrid structure in terms of the conversion efficiencies. Nonetheless, this approach can be employed when the coherence length L_c is increased by adjusting the structural parameters of the hybrid structure and λ_p.

IV. CONCLUSION

This paper proposes the GADC-based QPM approach and describes the analysis method for the hybrid structure based on this concept. The analysis of the hybrid structure demonstrates the feasibility of the GADC-based QPM. The analysis results demonstrate that the FWM facilitated by the GADC-based QPM leads to the efficient generation of the idler TE_S and TE_N modes with the pump TE_S mode and signal TE_S mode, especially when the Si strip width modulation is selected such that the coupling length is almost half the coherence length. The generated idler TE_N mode has a power comparable to that of the pump TE_N mode, and the generated mid-IR light can be effectively extracted from the SiN strip with the pump light highly suppressed. Owing to the characteristics of the GADC over a large number of periods, the conversion bandwidth is narrow. The disadvantage of the narrow bandwidth can be overcome through thermal tuning. In addition to the mid-IR generation, the mid-IR detection using the hybrid structure is discussed. The hybrid structure is advantageous because an additional combiner is not required to merge mid-IR light and pump light: The former and latter are coupled to the SiN and Si strips, respectively.

These results demonstrate that the GADC-based QPM facilitates efficient FWM in a Si waveguide with the standard thickness (*i.e.*, 220 nm) even when the difference between the idler and signal wavelengths is large. In addition, the hybrid structure based on the GADC-based QPM is promising for mid-IR generation and detection based on well-developed O-band and L-band sources and detectors.

V. APPENDIX

A. NONLINEAR COUPLED-MODE EQUATIONS

For the NCMEs, the electric and magnetic fields of the modes can be specified as

$$\mathbf{E}_{m(\nu)}(x,y,z) = A_{m(\nu)}(z)\frac{\mathbf{e}_{m(\nu)}(x,y)}{\sqrt{P_{m(\nu)}}}e^{-j\beta_{m(\nu)}z}, \tag{5a}$$

$$\mathbf{H}_{m(\nu)}(x,y,z) = A_{m(\nu)}(z)\frac{\mathbf{h}_{m(\nu)}(x,y)}{\sqrt{P_{m(\nu)}}}e^{-j\beta_{m(\nu)}z}, \tag{5b}$$

where $A_{m(\nu)}$ and $\beta_{m(\nu)}$ are the amplitude (in $\sqrt{\mathrm{W}}$) and propagation constant of mode m at λ_ν, respectively. For the TE$_\mathrm{S}$ and TE$_\mathrm{N}$ modes in section 1 (2), m is 1S and 1N (2S and 2N), respectively. For the pump, signal, and idler, ν is p, s, and i, respectively. The power carried by mode m, $P_{m(\nu)}$, is defined as $P_{m(\nu)} = \frac{1}{2}\int_{\mathrm{A}_\infty}\mathrm{d}x\mathrm{d}y\left(\mathbf{e}_{m(\nu)}\times\mathbf{h}^*_{m(\nu)}\right)\cdot\hat{z}$, where A_∞ denotes the cross-section area of the hybrid structure. In section l (l = 1 or 2), the NCMEs for the amplitudes of the TE$_\mathrm{S}$ modes can be expressed as

$$\begin{aligned}\frac{\mathrm{d}A_{l\mathrm{S(p)}}}{\mathrm{d}z} =& -j\frac{2\pi}{\lambda_\mathrm{p}}n_{l\mathrm{f(p)}}\Gamma^\mathrm{f}_{l\mathrm{S(p)}}A_{l\mathrm{S(p)}} \\ &-\frac{1}{2}\left(\alpha_{l\mathrm{S(p)}}+\alpha_{l\mathrm{f(p)}}\Gamma^\mathrm{f}_{l\mathrm{S(p)}}\right)A_{l\mathrm{S(p)}} \\ &-j\gamma^\mathrm{K}_{(\mathrm{p})}\left(\Gamma_{l\mathrm{S(p'pp'p)}}{}^\mathrm{K}\left|A_{l\mathrm{S(p)}}\right|^2+\Gamma^\mathrm{K}_{l\mathrm{S(p'ss'p)}}\left|A_{l\mathrm{S(s)}}\right|^2 \right.\\ &\left.\quad+\Gamma^\mathrm{K}_{l\mathrm{S(p'ii'p)}}\left|A_{l\mathrm{S(i)}}\right|^2\right)A_{l\mathrm{S(p)}} \\ &-j2\gamma^\mathrm{K}_{(\mathrm{p})}\Gamma^\mathrm{K}_{l\mathrm{S(p'p'si)}}A^*_{l\mathrm{S(p)}}A_{l\mathrm{S(s)}}A_{l\mathrm{S(i)}}e^{j\Delta\beta_{l\mathrm{S}}z},\end{aligned} \tag{6a}$$

$$\begin{aligned}\frac{\mathrm{d}A_{l\mathrm{S(s)}}}{\mathrm{d}z} =& -j\frac{2\pi}{\lambda_\mathrm{s}}n_{l\mathrm{f(s)}}\Gamma^\mathrm{f}_{l\mathrm{S(s)}}A_{l\mathrm{S(s)}} \\ &-\frac{1}{2}\left(\alpha_{l\mathrm{S(s)}}+\alpha_{l\mathrm{f(s)}}\Gamma^\mathrm{f}_{l\mathrm{S(s)}}\right)A_{l\mathrm{S(s)}} \\ &-j\gamma^\mathrm{K}_{(\mathrm{s})}\left(\Gamma^\mathrm{K}_{l\mathrm{S(s'ss's)}}\left|A_{l\mathrm{S(s)}}\right|^2+\Gamma^\mathrm{K}_{l\mathrm{S(s'pp's)}}\left|A_{l\mathrm{S(p)}}\right|^2 \right.\\ &\left.\quad+\Gamma^\mathrm{K}_{l\mathrm{S(s'ii's)}}\left|A_{l\mathrm{S(i)}}\right|^2\right)A_{l\mathrm{S(s)}} \\ &-j\gamma^\mathrm{K}_{(\mathrm{s})}\Gamma^\mathrm{K}_{l\mathrm{S(s'ppi')}}A^2_{l\mathrm{S(p)}}A^*_{l\mathrm{S(i)}}e^{-j\Delta\beta_{l\mathrm{S}}z},\end{aligned} \tag{6b}$$

$$\begin{aligned}\frac{\mathrm{d}A_{l\mathrm{S(i)}}}{\mathrm{d}z} =& -j\frac{2\pi}{\lambda_\mathrm{i}}n_{l\mathrm{f(i)}}\Gamma^\mathrm{f}_{l\mathrm{S(i)}}A_{l\mathrm{S(i)}} \\ &-\frac{1}{2}\left(\alpha_{l\mathrm{S(i)}}+\alpha_{l\mathrm{f(i)}}\Gamma^\mathrm{f}_{l\mathrm{S(i)}}\right)A_{l\mathrm{S(i)}} \\ &-j\gamma^\mathrm{K}_{(\mathrm{i})}\left(\Gamma^\mathrm{K}_{l\mathrm{S(i'ii'i)}}\left|A_{l\mathrm{S(i)}}\right|^2+\Gamma^\mathrm{K}_{l\mathrm{S(i'pp'i)}}\left|A_{l\mathrm{S(p)}}\right|^2 \right.\\ &\left.+\Gamma^\mathrm{K}_{l\mathrm{S(i'ss'i)}}\left|A_{l\mathrm{S(s)}}\right|^2\right)A_{l\mathrm{S(i)}} \\ &-j\gamma^\mathrm{K}_{(\mathrm{i})}\Gamma^\mathrm{K}_{l\mathrm{S(i'pps')}}A^2_{l\mathrm{S(p)}}A^*_{l\mathrm{S(s)}}e^{-j\Delta\beta_{l\mathrm{S}}z}.\end{aligned} \tag{6c}$$

In (6), $n_{l\mathrm{f}(\nu)}$ and $\alpha_{l\mathrm{f}(\nu)}$ pertain to the free-carrier index change and absorption in the Si strip of section l, expressed as $n_{l\mathrm{f}(\nu)} = -(\lambda_\nu/\lambda_\mathrm{r})^2(8.8\times10^{-4}N_l + 8.5N_l^{0.8})\times10^{-18}$ and $\alpha_{l\mathrm{f}(\nu)} = (\lambda_\nu/\lambda_\mathrm{r})^2 14.5\times10^{-18}N_l$, respectively [2], [16]. λ_r is the reference wavelength set at 1.55 μm, and N_l is the carrier density (in cm^{-3}) generated by the two photon absorption (TPA). N_l is calculated as $N_l = \tau_0\beta_\mathrm{T}\Gamma^\mathrm{K}_{l\mathrm{S(p'pp'p)}}\left|A_{l\mathrm{S(p)}}\right|^4\lambda_\mathrm{p}/(2hc\mathrm{A}_{l\mathrm{S}})$ [16], where τ_0, β_T, h, and $\mathrm{A}_{l\mathrm{S}}$ are the carrier lifetime (set at 1 ns), TPA coefficient, Planck constant, and area of the Si strip of section l, respectively. The linear absorption coefficient of the TE$_\mathrm{S}$ mode in section l at λ_ν, $\alpha_{l\mathrm{S}(\nu)}$, is mainly attributable to fabrication-caused scattering (notably, the materials in this study are assumed to be lossless). $\gamma^\mathrm{K}_{(\nu)}$ is the Kerr nonlinear coefficient specified as $\gamma^\mathrm{K}_{(\nu)} = 2\pi n_2/\lambda_\nu - j\beta_\mathrm{T}/2$ [3]. The nonlinear refractive index of Si, n_2, is 6×10^{-5} cm^2/GW [16], [17], and β_T is 0.45 cm/GW [16], [17]. The overlap factors $\Gamma^\mathrm{f}_{l\mathrm{S}(\nu)}$ and $\Gamma^\mathrm{K}_{l\mathrm{S}(\nu_1\nu_2\nu_3\nu_4)}$ are expressed as

$$\Gamma^\mathrm{f}_{l\mathrm{S}(\nu)} = \frac{1}{2}c\varepsilon_0 n_{\mathrm{S}(\nu)}\frac{1}{P_{l\mathrm{S}(\nu)}}\int_{\mathrm{A}_{l\mathrm{S}}}\mathrm{d}x\mathrm{d}y\left|\mathbf{e}_{l\mathrm{S}(\nu)}\right|^2, \tag{7}$$

and

$$\begin{aligned}\Gamma^\mathrm{K}_{l\mathrm{S}(\nu_1\nu_2\nu_3\nu_4)} =& \frac{\varepsilon_0^2c^2n^2_{\mathrm{S}(\nu_1)}}{4}\frac{1}{\sqrt{P_{l\mathrm{S}(\nu_1)}P_{l\mathrm{S}(\nu_2)}P_{l\mathrm{S}(\nu_3)}P_{l\mathrm{S}(\nu_4)}}} \\ &\times\int_{A_{l\mathrm{S}}}\mathrm{d}x\mathrm{d}y\ \mathbf{e}_{l\mathrm{S}(\nu_1)}\cdot\xi^{(3)}\vdots\mathbf{e}_{l\mathrm{S}(\nu_2)}\mathbf{e}_{l\mathrm{S}(\nu_3)}\mathbf{e}_{l\mathrm{S}(\nu_4)},\end{aligned} \tag{8}$$

respectively, where $n_{\mathrm{S}(\nu)}$ is the refractive index of Si at λ_ν [30]. If the wavelength index ν_i is presented with a prime symbol, $\mathbf{e}_{l\mathrm{S}(\nu_i)}$ in (8) must be conjugated. $\xi^{(3)}$ is the normalized third-order nonlinear susceptibility, each element of which is expressed as $\xi^{(3)}_{abcd} = \rho(\delta_{ab}\delta_{cd}+\delta_{ac}\delta_{bd}+\delta_{ad}\delta_{bc})/3+(1-\rho)\delta_{abcd}$ [2]. δ denotes the Kronecker delta, and ρ is 1.27 [2]. The integration in (7) and (8) is limited to the Si strip area because the TE$_\mathrm{S}$ mode is well confined in the Si strip (the confinement factor in the Si and SiN strips at a wavelength of 1.58 μm is 78.4 % and only 0.009 %, respectively). Moreover, SiN does not exhibit the free-carrier index change and absorption and TPA, and its n_2 is approximately 20 times smaller than $n_2$of Si [8]. Moreover, the TE$_\mathrm{N}$ modes at λ_p and λ_s are negligibly excited by the grating. Owing to these two aspects, nonlinear interactions among the TE$_\mathrm{N}$ modes or TE$_\mathrm{S}$ and TE$_\mathrm{N}$ modes are not considered.

B. CONVERSION EFFICIENCY CHANGES

To determine the variations of C$_\mathrm{S}$ and C$_\mathrm{N}$ along the z axis, C$_\mathrm{S}(z)$ and C$_\mathrm{N}(z)$, the amplitudes of the idler TE$_\mathrm{S}$ and TE$_\mathrm{N}$ modes for $\lambda_{\mathrm{s,peak}}$ are calculated with respect to z, squared, and normalized to the initial power of the signal TE$_\mathrm{S}$ mode. C$_\mathrm{S}(z)$ and C$_\mathrm{N}(z)$ for Δw = 25 nm, 50 nm, and 75 nm are shown in Fig. 8, along with C$_\mathrm{S}(z)$ obtained from the uniform composite waveguide without the grating.

When Δw = 25 nm, the power of the idler TE$_\mathrm{S}$ mode, generated by the FWM, is gradually but sufficiently transferred to the idler TE$_\mathrm{N}$ mode in the interval $0 \le z \le L_\mathrm{c}$

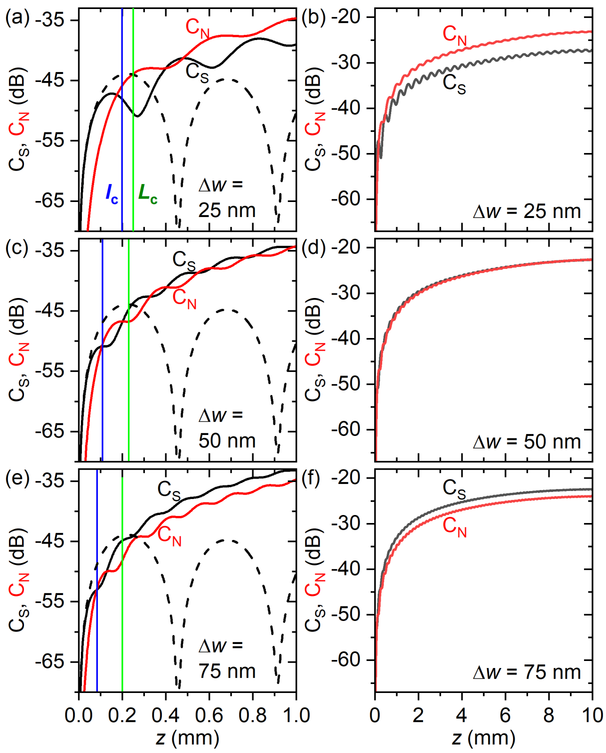

FIGURE 8. **Changes of the conversion efficiencies C_S (black curves) and C_N (red curves) along the hybrid structure. In (a), (c), and (e), the black dashed curves show C_S in the uniform composite waveguide without the grating. The vertical blue and green lines indicate the coupling length l_c and coherence length L_c, respectively. (a) and (b) are calculated for Δw = 25 nm, λ_S = 1.2612 μm, and Λ_2 = 2.824 μm; (c) and (d) for Δw = 50 nm, λ_S = 1.2601 μm, and Λ_2 = 2.554 μm; (e) and (f) for Δw = 75 nm, λ_S = 1.2590 μm, and Λ_2 = 2.352 μm. The other parameters are the same as those in the case shown in Fig. 4.**

because l_c is similar to L_c. Consequently, C_S decreases to the local minimum near L_c, and C_N increases to a large value. Because of the FWM facilitated by the GADC, C_S increases again as z increases from L_c, which is different from the large decrease in C_S without the grating for z between L_c and $2L_c$. The increased power of the idler TE_S mode is effectively transferred to the idler TE_N mode, and C_N increases in the interval $L_c \leq z \leq 2L_c$. Consequently, the degree of increase in C_N is more than that in C_S along the hybrid structure.

When Δw = 50 nm, the GADC leads to an increase in C_N, and the value of C_N approaches that of C_S at l_c. Because $l_c \approx L_c/2$, the idler TE_S mode is efficiently generated in the interval $l_c \leq z \leq L_c$. C_S does not decrease near l_c and increases again in that interval, which is different from the trend of C_S for $\Delta w = 25$ nm. For $z > L_c$, C_S increases owing to the FWM, and C_N increases to the level of C_S owing to the GADC. In this manner, the increasing trends of C_S and C_N along the hybrid structure are similar.

When Δw = 75 nm, $l_c < L_c/2$. The idler TE_S mode is weakly generated by the FWM in the interval $0 \leq z \leq l_c$. In this interval, the generated power of the idler TE_S mode is sufficiently transferred to the idler TE_N mode, and C_N is nearly equal to C_S at l_c. The interval $l_c \leq z \leq L_c$ is wider than in the case of Δw = 50 nm. Hence, as z increases from l_c to L_c, the idler TE_S mode is more efficiently generated by the FWM than in the case of Δw = 50 nm. In this interval, C_S continuously increases, and the difference in C_S and C_N at L_c is larger than that for Δw = 50 nm. For $z > L_c$, the FWM increases C_S more than the GADC increases C_N. Consequently, C_S increases more than C_N along the hybrid structure.

REFERENCES

[1] M. A. Foster, A. C. Turner, J. E. Sharping, B. S. Schmidt, M. Lipson, and A. L. Gaeta, "Broad-band optical parametric gain on a silicon photonic chip," *Nature*, vol. 441, pp. 960–963, Jun. 2006.

[2] Q. Lin, O. J. Painter, and G. P. Agrawal, "Nonlinear optical phenomena in silicon waveguides: Modeling and applications," *Opt. Exp.*, vol. 15, no. 25, pp. 16604–16644, Dec. 2007.

[3] R. M. Osgood, N. C. Panoiu, J. I. Dadap, X. Liu, X. Chen, I.-W. Hsieh, E. Dulkeith, W. M. J. Green, and Y. A. Vlasov, "Engineering nonlinearities in nanoscale optical systems: Physics and applications in dispersion-engineered silicon nanophotonic wires," *Adv. Opt. Photon.*, vol. 1, no. 1, pp. 162–235, Jan. 2009.

[4] J. Leuthold, C. Koos, and W. Freude, "Nonlinear silicon photonics," *Nature Photon.*, vol. 4, pp. 535–544, Aug. 2010.

[5] A. C. Turner-Foster, M. A. Foster, R. Salem, A. L. Gaeta, and M. Lipson, "Frequency conversion over two-thirds of an octave in silicon nanowaveguides," *Opt. Exp.*, vol. 18, no. 3, pp. 1904–1908, Feb. 2010.

[6] X. Liu, B. Kuyken, G. Roelkens, R. Baets, R. M. Osgood, and W. M. J. Green, "Bridging the mid-infrared-to-telecom gap with silicon nanophotonic spectral translation," *Nature Photon.*, vol. 6, no. 10, pp. 667–671, Oct. 2012.

[7] M. Borghi, C. Castellan, S. Signorini, A. Trenti, and L. Pavesi, "Nonlinear silicon photonics," *J. Opt.*, vol. 19, no. 9, Sep. 2017, Art. no. 093002.

[8] K. Li and A. C. Foster, "Parametric nonlinear silicon-based photonics," *Proc. IEEE*, vol. 106, no. 12, pp. 2196–2208, Dec. 2018.

[9] E.-K. Tien, Y. Huang, S. Gao, Q. Song, F. Qian, S. K. Kalyoncu, and O. Boyraz, "Discrete parametric band conversion in silicon for mid-infrared applications," *Opt. Exp.*, vol. 18, no. 21, pp. 21981–21989, Oct. 2010.

[10] B. Kuyken, P. Verheyen, P. Tannouri, X. Liu, J. Van Campenhout, R. Baets, W. M. J. Green, and G. Roelkens, "Generation of 3.6 μm radiation and telecom-band amplification by four-wave mixing in a silicon waveguide with normal group velocity dispersion," *Opt. Lett.*, vol. 39, no. 6, pp. 1349–1352, Mar. 2014.

[11] X. Li, P. Zhou, S. He, and S. Gao, "Dispersion engineering of suspended silicon photonic waveguides for broadband mid-infrared wavelength conversion," *J. Opt. Soc. Amer. B, Opt. Phys.*, vol. 31, no. 10, pp. 2295–2301, Oct. 2014.

[12] D. Lyu, Q. Jin, and S. Gao, "Design of mid-infrared nonlinear silicon-germanium waveguides for broadband/discrete-band wavelength conversion," *J. Opt. Soc. Amer. B, Opt. Phys.*, vol. 35, no. 4, pp. 741–751, Apr. 2018.

[13] S. Signorini, M. Mancinelli, M. Borghi, M. Bernard, M. Ghulinyan, G. Pucker, and L. Pavesi, "Intermodal four-wave mixing in silicon waveguide," *Photon. Res.*, vol. 6, no. 8, pp. 805–814, Aug. 2018.

[14] J. B. Driscoll, N. Ophir, R. R. Grote, J. I. Dadap, N. C. Panoiu, K. Bergman, and R. M. Osgood, "Width-modulation of Si photonic wires for quasi-phase-matching of four-wave-mixing: Experimental and theoretical demonstration," *Opt. Exp.*, vol. 20, no. 8, pp. 9227–9242, Apr. 2012.

[15] S. Lavdas, S. Zhao, J. B. Driscoll, R. R. Grote, R. M. Osgood, and N. C. Panoiu, "Wavelength conversion and parametric amplification of optical pulses via quasi-phase-matched four-wave mixing in long-period Bragg silicon waveguides," *Opt. Lett.*, vol. 39, no. 13, pp. 4017–4020, Jul. 2014.

[16] Y. Lefevre, N. Vermeulen, and H. Thienpont, "Quasi-phase-matching of four-wave-mixing-based wavelength conversion by phase-mismatch switching," *J. Lightw. Technol.*, vol. 31, no. 13, pp. 2113–2121, Jul. 15, 2013.

[17] B. Jin, J. Yuan, C. Yu, X. Sang, S. Wei, X. Zhang, Q. Wu, and G. Farrell, "Efficient and broadband parametric wavelength conversion in a vertically etched silicon grating without dispersion engineering," *Opt. Exp.*, vol. 22, no. 6, pp. 6257–6268, Mar. 2014.

[18] X. Zhang, J. Yuan, J. Zou, B. Jin, X. Sang, Q. Wu, C. Yu, and G. Farrell, "Enhanced broadband parametric wavelength conversion in silicon waveguide with the multi-period grating," *IEEE Photon. J.*, vol. 6, no. 6, pp. 1–14, Dec. 2014.

[19] F. Zhou, M. Zhang, J. Dai, Y. Wang, L. Deng, and D. Liu, "Efficient and broadband wavelength conversion in a slot waveguide with the periodic structure altering the phase-mismatch," *Appl. Opt.*, vol. 54, no. 25, pp. 7753–7759, Sep. 2015.

[20] Y. Liu, C. Wu, X. Qiang, J. Wu, X. Yang, and P. Xu, "Evanescent-wave coupling phase-matching for ultrawidely tunable frequency conversion in silicon-waveguide chips," *Opt. Exp.*, vol. 27, no. 20, pp. 28866–28878, Sep. 2019.

[21] P. Dong and A. G. Kirk, "Nonlinear frequency conversion in waveguide directional couplers," *Phys. Rev. Lett.*, vol. 93, no. 13, Sep. 2004, Art. no. 133901.

[22] I. Biaggio, V. Coda, and G. Montemezzani, "Coupling-length phase matching for nonlinear optical frequency conversion in parallel waveguides," *Phys. Rev. A, Gen. Phys.*, vol. 90, no. 4, Oct. 2014, Art. no. 043816.

[23] B. Liu, H. Yu, Z.-Y. Li, and L. Tong, "Phase-matched second-harmonic generation in coupled nonlinear optical waveguides," *J. Opt. Soc. Amer. B, Opt. Phys.*, vol. 36, no. 10, pp. 2650–2658, Oct. 2019.

[24] W. D. Sacher, Y. Huang, G. Lo, and J. K. S. Poon, "Multilayer silicon nitride-on-silicon integrated photonic platforms and devices," *J. Lightw. Technol.*, vol. 33, no. 4, pp. 901–910, Feb. 15, 2015.

[25] J. C. C. Mak, Q. Wilmart, S. Olivier, S. Menezo, and J. K. S. Poon, "Silicon nitride-on-silicon bi-layer grating couplers designed by a global optimization method," *Opt. Exp.*, vol. 26, no. 10, pp. 13656–13665, May 2018.

[26] A. Yariv and P. Yeh, *Photonics: Optical Electronics in Modern Communications*, 6th ed. New York, NY, USA: Oxford, 2007, pp. 125–126.

[27] J. M. C. Boggio, D. Bodenmüller, T. Fremberg, R. Haynes, M. M. Roth, R. Eisermann, M. Lisker, L. Zimmermann, and M. Böhm, "Dispersion engineered silicon nitride waveguides by geometrical and refractive-index optimization," *J. Opt. Soc. Amer. B, Opt. Phys.*, vol. 31, no. 11, pp. 2846–2857, Nov. 2014.

[28] S. K. Selvaraja, W. Bogaerts, P. Dumon, D. V. Thourhout, and R. Baets, "Subnanometer linewidth uniformity in silicon nanophotonic waveguide devices using CMOS fabrication technology," *IEEE J. Sel. Topics Quantum Electron.*, vol. 16, no. 1, pp. 316–324, Jan./Feb. 2010.

[29] C. Porzi, G. J. Sharp, M. Sorel, and A. Bogoni, "Silicon photonics high-order distributed feedback resonators filters," *IEEE J. Quantum Electron.*, vol. 56, no. 1, pp. 1–9, Feb. 2020.

[30] N. C. Panoiu, J. F. Mcmillan, and C. Wei Wong, "Theoretical analysis of pulse dynamics in silicon photonic crystal wire waveguides," *IEEE J. Sel. Topics Quantum Electron.*, vol. 16, no. 1, pp. 257–266, Jan./Feb. 2010.

MIN-SUK KWON received the B.S. *(summa cum laude)*, M.S., and Ph.D. degrees in electrical engineering from the Korea Advanced Institute of Science and Technology (KAIST), Daejeon, South Korea, in 1998, 2000, and 2005, respectively. He was a Postdoctoral Research Associate at KAIST and the University of Southern California. In September 2007, he joined the Department of Optical Engineering of Sejong University as a Full-Time Lecturer. In March 2009, he became an Assistant Professor, and worked there until January 2012. Since January 2012, he has been working as an Associate Professor with the Department of Electrical Engineering, Ulsan National Institute of Science and Technology (UNIST). He did active researches on thermo-optically induced long-period gratings. He has been studying integrated-optical devices such as micro-ring resonators, long-period waveguide gratings, and silicon photonic waveguide modulators and photodetectors. He strongly focuses on development of nanoplasmonic waveguide devices, graphene-based waveguide devices, and graphene plasmon devices working in the mid-infrared.